



OPEN ACCESS

EDITED BY

Jian Wu,
Harbin Institute of Technology, China

REVIEWED BY

Esraa N. Thabet,
Sohag University, Egypt
Mir Irfan Ul Haq,
Shri Mata Vaishno Devi University, India

*CORRESPONDENCE

Andrea Montalti,
✉ andrea.montalti8@unibo.it

RECEIVED 17 April 2023

ACCEPTED 27 June 2023

PUBLISHED 18 July 2023

CITATION

Ferretti P, Pagliari C, Montalti A and
Liverani A (2023), Design and
development of a peristaltic pump for
constant flow applications.
Front. Mech. Eng 9:1207464.
doi: 10.3389/fmech.2023.1207464

COPYRIGHT

© 2023 Ferretti, Pagliari, Montalti and
Liverani. This is an open-access article
distributed under the terms of the
[Creative Commons Attribution License
\(CC BY\)](https://creativecommons.org/licenses/by/4.0/). The use, distribution or
reproduction in other forums is
permitted, provided the original author(s)
and the copyright owner(s) are credited
and that the original publication in this
journal is cited, in accordance with
accepted academic practice. No use,
distribution or reproduction is permitted
which does not comply with these terms.

Design and development of a peristaltic pump for constant flow applications

Patrich Ferretti, Curzio Pagliari, Andrea Montalti* and
Alfredo Liverani

Department of Industrial Engineering, Alma Mater Studiorum University of Bologna, Bologna, Italy

In wide-ranging areas, including hydraulics, biomedical, automotive, and aerospace, there is often a need to move a fluid with a constant flow rate. This is difficult to achieve with any type of pump and usually other elements are inserted to regularize the output. This study focused on the peristaltic pump because there are few studies on it and it has some interesting features, such as extreme simplicity, a small number of components, and the extreme compactness of the whole system. The first part of this study is focused on analyzing the classical geometry of the peristaltic pump to understand the origin of the discontinuity in the flow rate; the second part proposes a new geometry that mitigates the flow irregularity by more than 200%. In this way, it is possible to use it in all the sectors where a constant flow rate is required but where insulation between the fluid and the machine is required. Together with the flow study, an analysis of how the main geometric parameters affect the operation of the pump is provided, complete with explanatory graphs and tables. A prototype made through additive manufacturing technologies is also proposed.

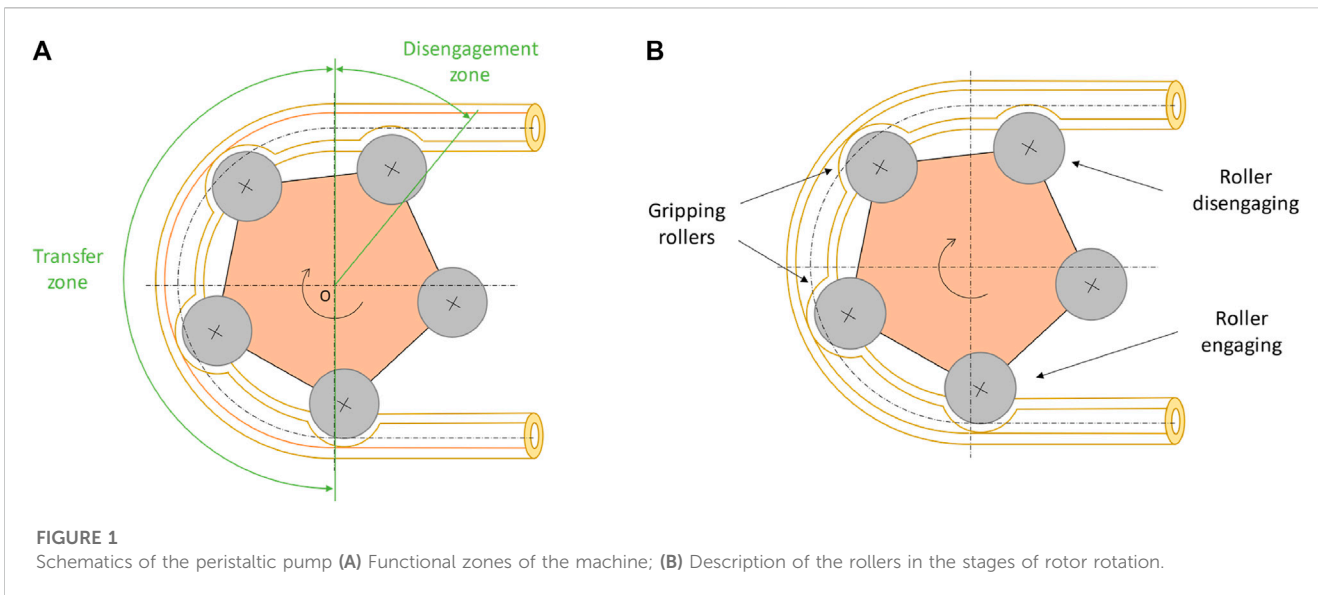
KEYWORDS

peristaltic pump, constant flow rate, 3D printing, calculation, fluid transfer

1 Introduction to the peristaltic pump

The peristaltic pump applies the principle of peristalsis (Jaffrin and Shapiro, 1971; Turton, 1994), whereby the prevalence of the treated fluid is imposed by a restriction running along the pipe (Weinberg et al., 1971; El-Din and Rabi, 2009). The pump consists of a rotor to which two or more rollers are attached, which rotate to throttle the pipe against the case isolating a volume of fluid and transferring it from the suction to the discharge (Latham, 1966; Shapiro et al., 1969; Karassik et al., 2008). Depending on the type of fluid, the element that chokes the pipe changes. For fluids with solid elements in suspension, skids are used while for fluids without solid particles, rollers are utilized (Saunier et al., 2022).

These pumps are widely used in all the processes where there is a requirement that the fluid should not meet machine components (Volk, 2013), for example, in the medical (Kunz et al., 1997; Khandpur, 2003), chemical (Farooq and Hussain, 2022), pharmaceutical (Abd-Alla et al., 2022a), or food industries (Liu et al., 2018). The dimensions vary according to the application (Formato et al., 2018), the nominal flow rate, and the type of fluid to be handled; they vary from tubes with an internal diameter of 2 mm for low-density fluids with no suspended particles, to tubes of 130 mm for high flow rates and transport of fluids with suspended bodies (Chakraborty et al., 2012). The number of rollers in commercially available pumps is usually 2 or 3. Small pumps are made with plastic components because they are lighter and cheaper, also they have to withstand a smaller number of operating hours; large



pumps are made of metal materials to ensure good structural strength, proper operation given the forces involved, and a high number of operating hours (Elabbasi et al., 2011).

This article starts with the study of the classic peristaltic pump (Sausse, 2018) to study the pulsation generated by the fluid flow. It is one of the few pumps that allow the fluid to be isolated from the moving parts of the pump but in many sectors, they are forced to use other types because this behavior of the fluid is not permissible. Unlike other works in the literature (Abd-Alla et al., 2021; Bayones et al., 2021; Abd-Alla et al., 2022b; Bayones et al., 2022; Abd-Alla et al., 2022c; Abd-Alla A. M. et al., 2022; Abd-Alla et al., 2023a; Abd-Alla et al., 2023b) regarding the geometry of the machine (Kaplan et al., 2018), it was possible to obtain a constant flow rate (Formato et al., 2019) without losing performance and finally, a prototype was created using 3D printing technology (Dave and Davim, 2021; Hsu et al., 2022).

1.1 Introduction to FDM for the realization of functional parts

FDM is the most renowned 3D printing method in the market (Kristiawan et al., 2021) due to the variety of possible printable materials from mainstream PLA (Arockiam et al., 2022) to more professional materials such as nylons, reinforced polymers (Wickramasinghe et al., 2020) such as carbon fiber and ABS, and up to engineering materials such as Polyether ether ketone (PEEK) (Wang et al., 2020) and Polypropylene (PP) (Bachhar et al., 2020). 3D printing has been known for its ability in creating complex geometries at low costs, especially for rapid prototyping applications (Kafle et al., 2021). Nevertheless, FDM methodologies are still challenging as their exterior surface quality and internal structure (Kumar et al., 2022) makes these products difficult to be standardized for mechanical applications (Wickramasinghe et al., 2020). Moreover, because of the technology, they result in low productivity (Raza et al., 2022) while they prove to be solid for low-cost end-use parts and

small-lot production (Rouf et al., 2022). FDM printing processes have many fields of applications: biomedical (Frizziero et al., 2022a), tissue engineering, human bone repair (Alessandri et al., 2022; Alessandri et al., 2023), antibacterial, bioprinting (Chaturvedi et al., 2022), electrical conductivity (Mora et al., 2020), electromagnetic, sensor, battery, automotive (Romero et al., 2021; Frizziero et al., 2022b; Frizziero et al., 2022c; Frizziero et al., 2023), aviation, smart textile (Chakraborty and Biswas, 2020), environmental, and luminescence applications among other areas (Jandyal et al., 2022).

1.2 Objectives

In summary, the objectives of the work are.

- find a geometry that allows a constant flow rate to be obtained;
- analyze how the flow varies as the geometric parameters of the pump vary;
- create a simple geometry composed of a few components.

2 Materials and methods

2.1 Displacement and flow rate of the classical peristaltic pump

A parameterization using geometric data that can be shared among various models of peristaltic pumps is presented and formulas and schematizations for calculating displacement and flow rate are then illustrated.

The peristaltic pump consists of a rotor to which two or more rollers are attached that rotate, squeezing the tube against the case, isolating a volume of fluid, and moving it from the suction to the discharge (Figure 1). Two zones of the machine are defined, the first is the “transfer zone” where the fluid is isolated and moved from the suction to the discharge and is 180° wide; the second is the

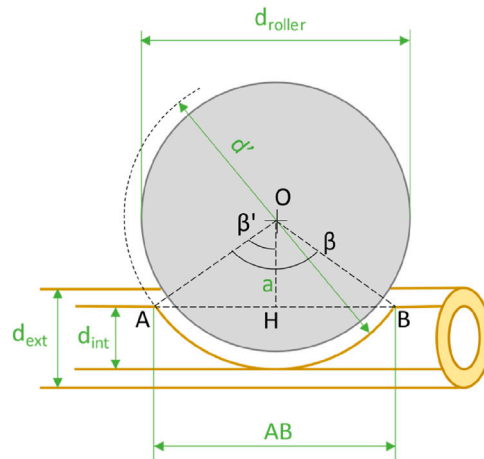


FIGURE 2
Diagram of machine and detail of a roller engaged on the tube.

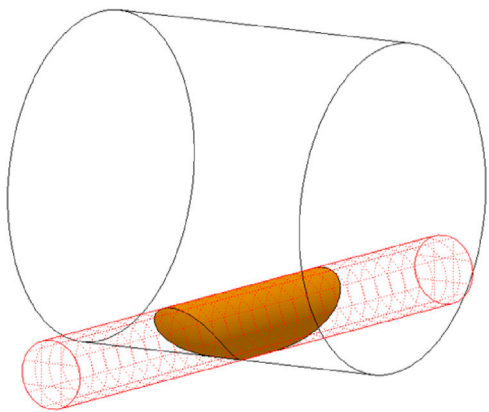


FIGURE 3
The volume given by the intersection of two cylinders with different diameters at skewed axes.

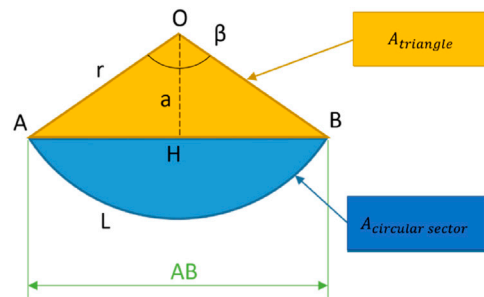


FIGURE 4
Diagram of the circular sector with construction parameters.

$$V_{tube\ int.} = CA_{int} = \pi D_{axis} \frac{\pi d_{int}^2}{4} = \frac{\pi^2 D_{axis} d_{int}^2}{4} \quad (3)$$

The volume occupied by the z rollers crushing the tube should be subtracted ($V_{element}$); following a full rotation, all the rollers engage once for one

$$V_{actual} = V_{tube\ int.} - z V_{element} \quad (4)$$

The volume occupied by the roller crushing the pipe, considering the pipe locally straight, is obtained from the intersection between two cylinders with different diameters at skewed axes. A schematization is presented in Figure 3.

To derive the volume of the fluid element, begin by calculating the area of the circular segment when the roller crushes the tube; this is done theoretically by considering a tube that adheres perfectly to the roller as depicted in the figure below.

Knowing that:

$$a = \frac{d'}{2} - d_{int} \quad (5)$$

$$d' = d_{roller} + (d_{ext} - d_{int}) \quad (6)$$

“disengagement zone,” consecutive to the first and defines the amplitude in which the roller moves away from the tube until it makes no contact.

Beginning with the calculation of the displacement, considering the internal volume of the tube running through the entire transfer zone, which will have to be multiplied by two to consider a full rotation of the rotor. C is the overall length of the circle defined by the middle diameter of the tube called: D_{axis} . A_{int} is the internal cross-section area of the tube, defined by the inner diameter d_{int} as reported in Figure 2.

$$C = \pi D_{axis} \quad (1)$$

$$A_{int} = \frac{\pi d_{int}^2}{4} \quad (2)$$

Using the two relationships, the internal volume of the tube ($V_{tube\ int.}$) is obtained:

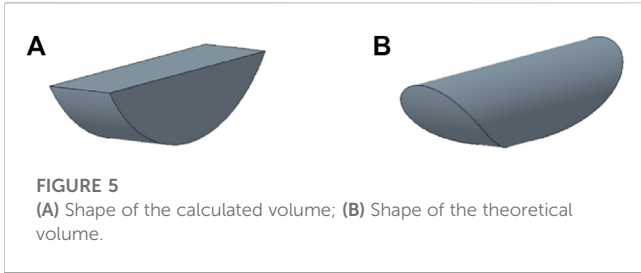


FIGURE 5
(A) Shape of the calculated volume; (B) Shape of the theoretical volume.

$$r = \frac{d'}{2} \tag{7}$$

Considering Figure 4, the Pythagorean theorem is applied to derive the segment AH:

$$AH = \sqrt{OA^2 - OH^2} = \sqrt{r^2 - a^2} \tag{8}$$

From which it is possible to derive the segment AB:

$$AB = 2\sqrt{r^2 - a^2} \tag{9}$$

Carnot's theorem on the AOH triangle:

$$AH^2 = a^2 + r^2 - 2ar \cos \beta' \tag{10}$$

From which the angle β' is derived:

$$\beta' = \arccos\left(\frac{a^2 + r^2 - AH^2}{2ar}\right) \tag{11}$$

Turning then to the β angle:

$$\beta = 2\arccos\left(\frac{a^2 + r^2 - AH^2}{2ar}\right) \tag{12}$$

With a simple proportion, the length of the arc of the circumference of the circular sector is calculated:

$$\frac{L}{2\pi r} = \frac{\beta}{360} \rightarrow L = \frac{\beta 2\pi r}{360} \tag{13}$$

Knowing that the area of the circular sector (yellow area + blue area in Figure 4) and the area of the triangle (yellow area in Figure 4) are:

$$A_{circular\ sector} = \frac{Lr}{2} \tag{14}$$

$$A_{triangle} = \frac{ABa}{2} \tag{15}$$

The area of the circular segment is easily derived:

$$A_{circular\ segment} = A_{circular\ sector} - A_{triangle} \tag{16}$$

To obtain the volume of the circular segment, one must multiply the area found by its depth, in this case, it is the inner diameter of the pipe. Mathematically, a solid is generated that has a rectangular cross-section along the longitudinal axis represented in Figure 5 on the left. The theoretical volume to be calculated is represented in Figure 5 on the right.

To arrive at an approximate solution of the volume sought, a corrective term is inserted into the element volume formula, which is

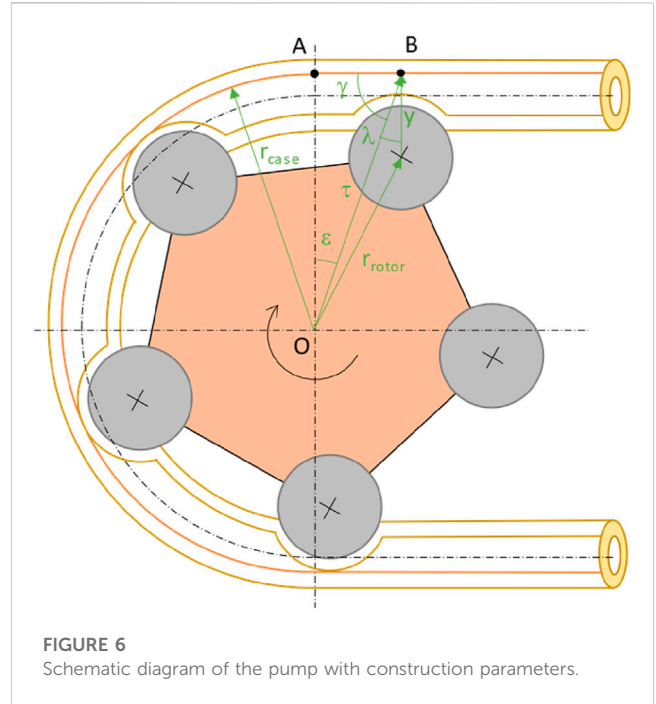


FIGURE 6
Schematic diagram of the pump with construction parameters.

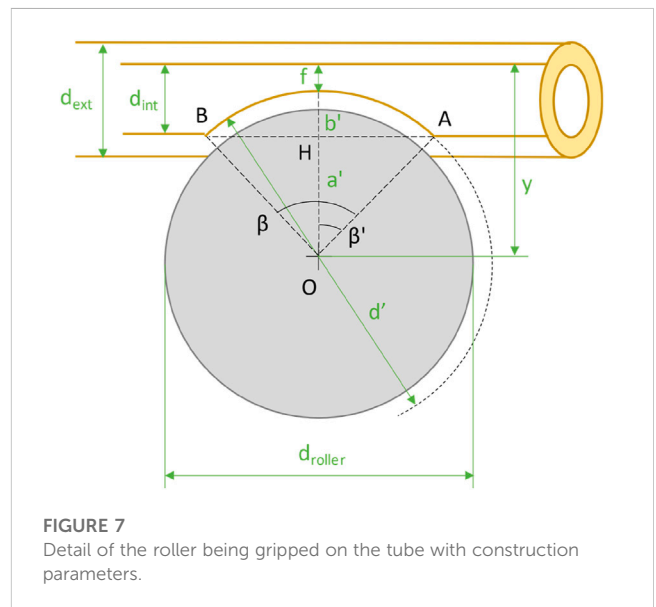


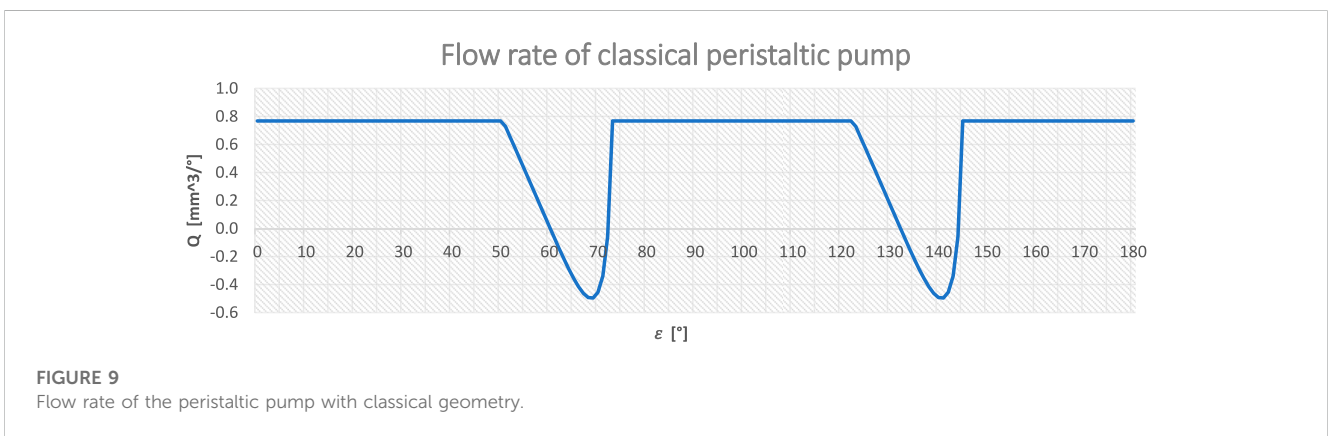
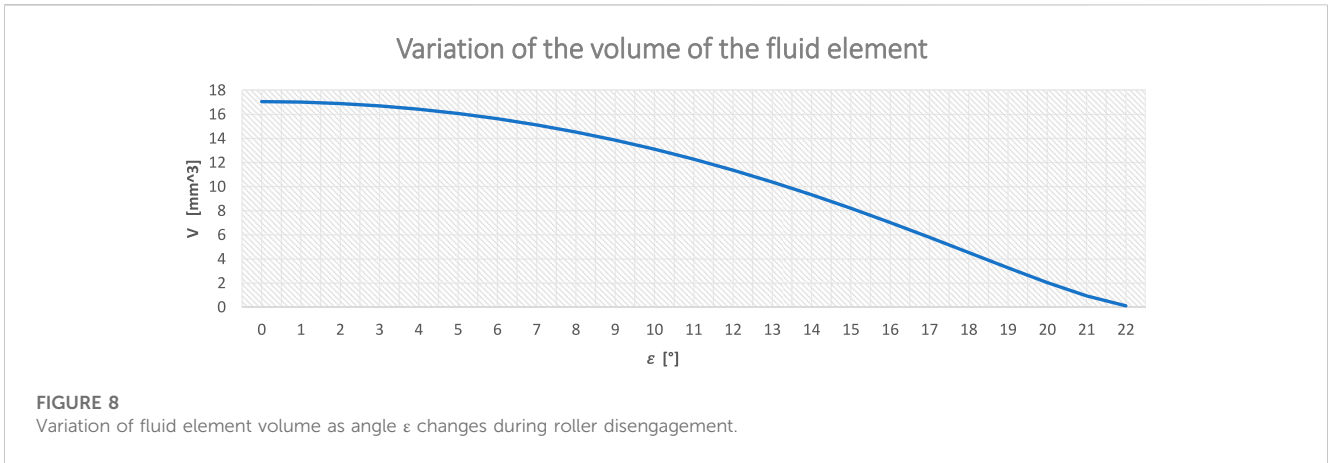
FIGURE 7
Detail of the roller being gripped on the tube with construction parameters.

the ratio of the area of the circle to the area of the square circumscribed by the circle.

$$\frac{A_{circle}}{A_{square}} = \frac{\pi}{4} \tag{17}$$

Through this procedure, the calculated volume differs by approximately 2% from the theoretical volume calculated through the CAD program.

For the exact calculation, one would have to perform a triple integral on the intersection volume of two cylinders with skewed axes and different diameters (similar to Steinmetz volume), it presents too much complexity for the intended purpose.



The volume of the circular segment will be:

$$V_{element} \cong A_{circular\ segment} d_{int} \frac{\pi}{4} \quad (18)$$

In conclusion, the displacement of the machine will be:

$$V_{actual} = V_{tube\ int} - 5V_{element} \quad (19)$$

Knowing the rated capacity and displacement of the machine, it is possible to derive the rotational speed of the motor to properly move the pump.

$$n_{max} = \frac{Q_{max}}{V_{actual}} 60 [rpm] \rightarrow \omega_{max} = \frac{n_{max} 2\pi}{60} [rad/s] \quad (20)$$

The flow rate has been made independent of the pump rotation speed, so all considerations and comparisons will be comparable without having to define a rotation speed.

To define the flow rate in this machine geometry, the volume of fluid moved with a rotation of one degree by the last fully engaged roller in the conveying zone is estimated, from which the change in volume due to the roller disengaging on the pipe must be subtracted.

As can be seen in Figure 6, the angle ϵ defines the angular position of the rotor; deriving the angle γ knowing that the sum of the interior angles of a triangle (AOB) always makes 180:

$$\gamma = 180 - (\epsilon + 90) \quad (21)$$

Knowing the AO side and the two angles ϵ and γ , the OB side called τ can be derived:

$$\tau = r_{case} \frac{\sin 90}{\sin \gamma} \quad (22)$$

Knowing the radius of the rotor, the cosine theorem is applied:

$$r_{rotor}^2 = \tau^2 + y^2 - 2\tau y \cos \lambda \quad (23)$$

To derive the parameter y that varies as the angle ϵ changes:

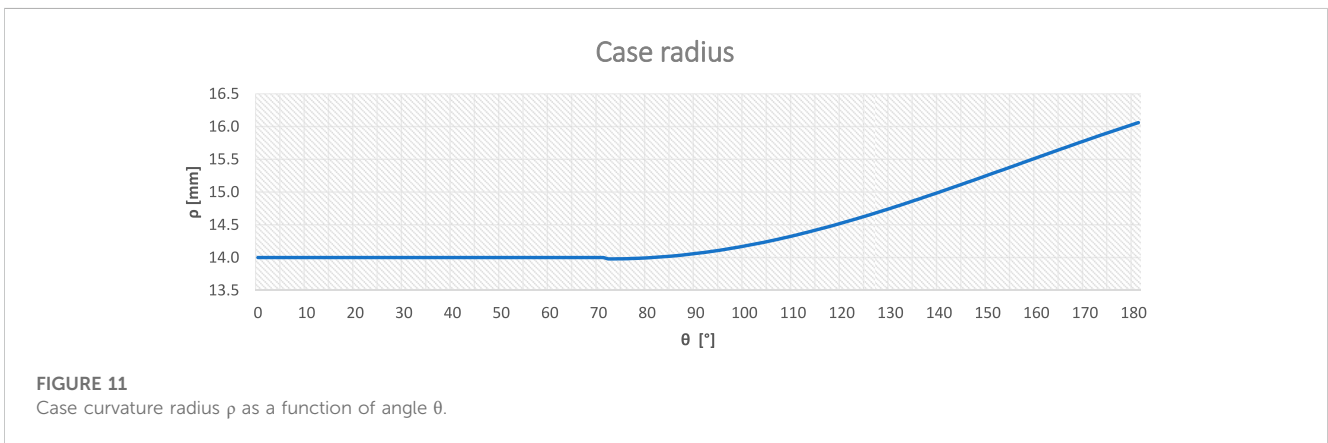
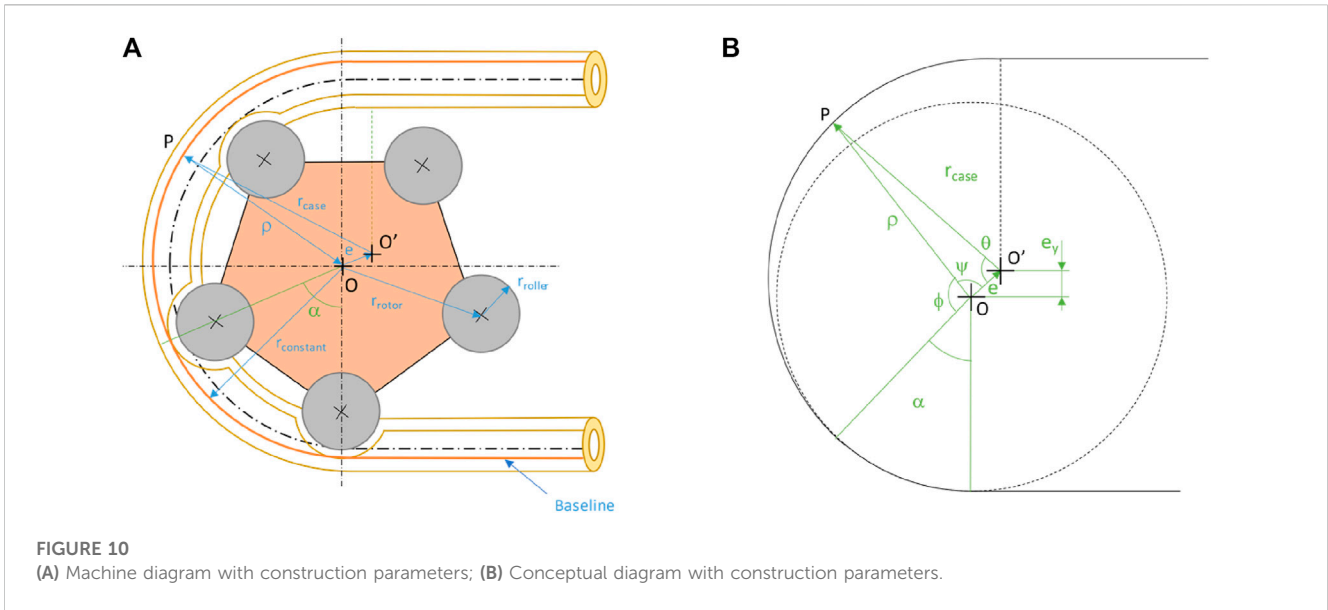
$$y = \tau \cos \lambda \pm \sqrt{\tau^2 (\cos \lambda)^2 - \tau^2 + r_{rotor}^2} \quad (24)$$

One must choose the negative sign otherwise it makes no physical sense.

Considering Figure 7, the distance y is used to obtain the parameter f , which is of interest until the roller completely disengages from the tube, and is obtained through the closure equation:

$$y = r_{roller} + f + \left(\frac{d_{ext} - d_{int}}{2} \right) \rightarrow f = y - r_{roller} - \left(\frac{d_{ext} - d_{int}}{2} \right) \quad (25)$$

Needed to derive the parameter a' , which at the point of last detachment will be equal to the radius of the roller:



$$b' = d_{int} - f \quad (26)$$

$$a' = y - b' - f \quad (27)$$

Once the parameter a' is obtained, one can proceed with the calculation of the volume occupied by the roller on the tube, as carried out for the calculation of the displacement. Starting from Eq. (8), AH (Figure 7) is obtained, to obtain β and arrive at the surface area value of the circular segment. The calculation of the volume of the fluid element is carried out as in Eq. (18). Plotting the trend on a graph, the curve shown in Figure 8 is obtained.

Knowing the volume occupied by the roller as the angle ϵ changes, the change in volume between one position (ϵ) and the next ($\epsilon + 1$) is calculated:

$$\Delta V_{element} = V_{element(\epsilon)} - V_{element(\epsilon+1)} \quad (28)$$

Finally, the change in volume of the liquid with one degree rotation is calculated:

$$\Delta V_{liquid 1^\circ} = l_{arc 1^\circ} \cdot A_{tube} = \frac{\Delta \epsilon \cdot 2\pi r_{case}}{360} \frac{\pi d_{tubo int}^2}{4} \quad (29)$$

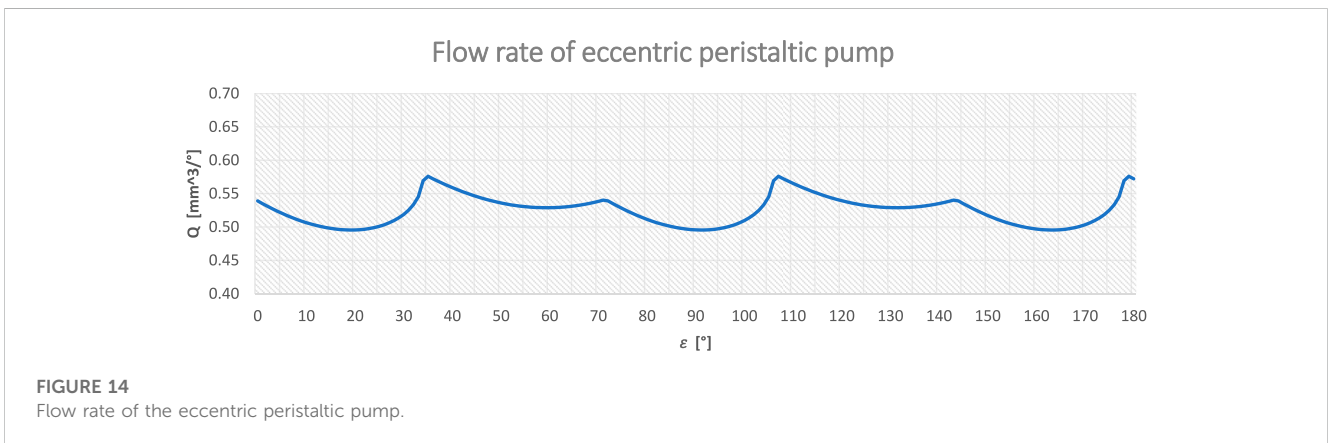
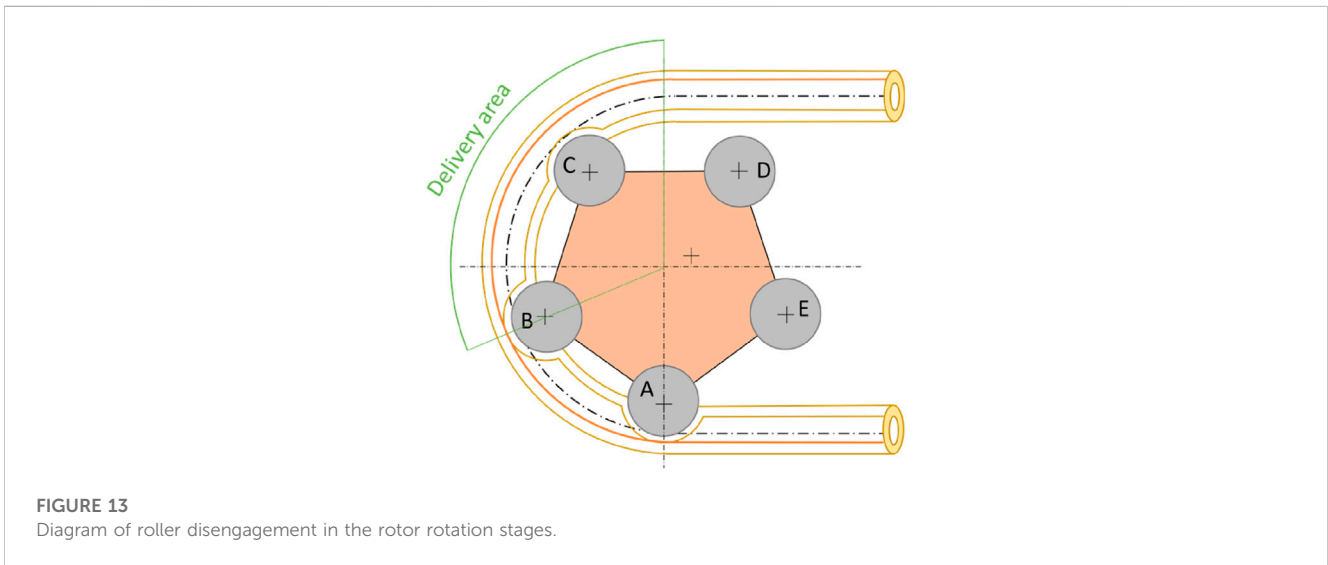
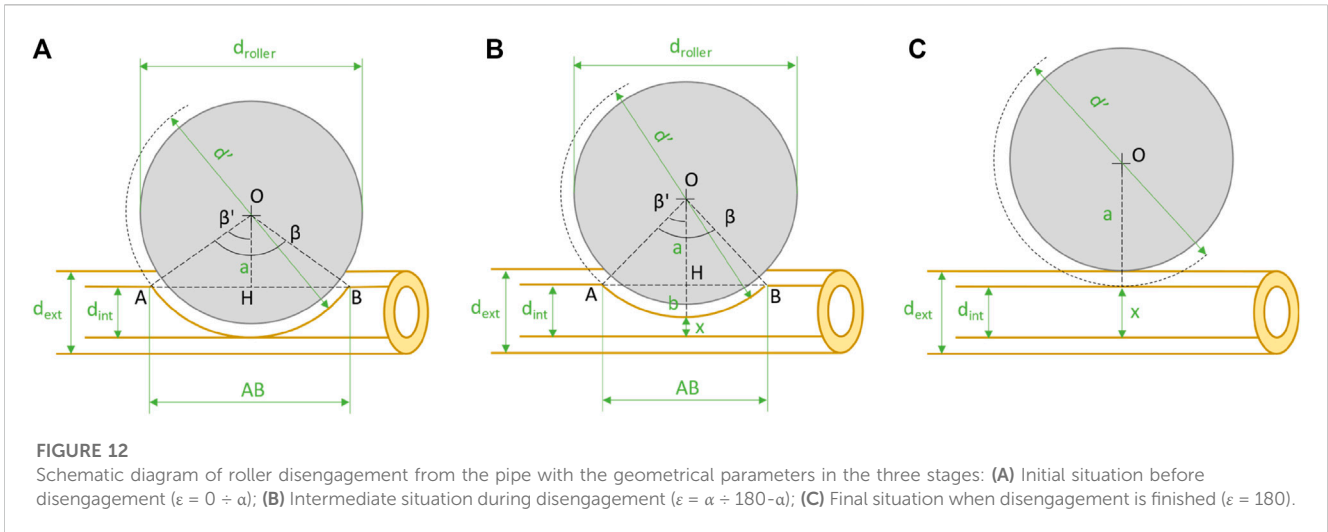
Considering:

$$l_{arc 1^\circ} = \frac{\pi D_{axis}}{360} \quad (30)$$

The flow rate of this pump has two phases.

- The first phase begins when the roller has finished the transfer arc and no longer completely occludes the pipe, generating a passage light for the fluid. From this moment, the roller disengagement phase begins and ends when there is no more contact between the roller and the pipe. The duration of this phase is approximately 22.
- The second phase begins at the end of the first one and is the remaining rotation that transfers fluid to the delivery with a constant trend until the next roller begins to disengage from the pipe.

The entire cycle repeats every $360/z$, where $z = 5$, so every 72. Putting this concept back into formulas, getting:



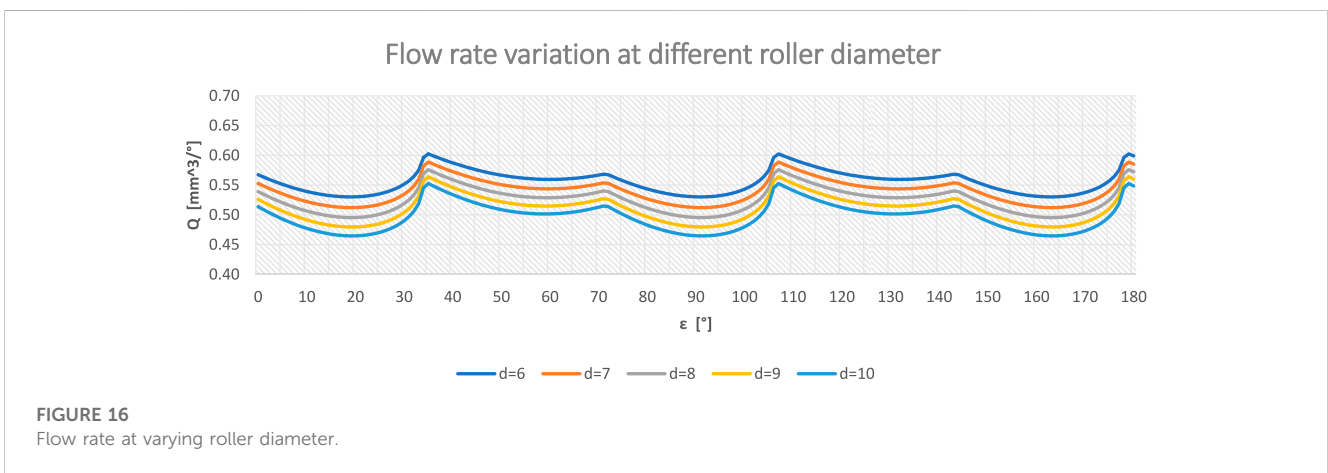
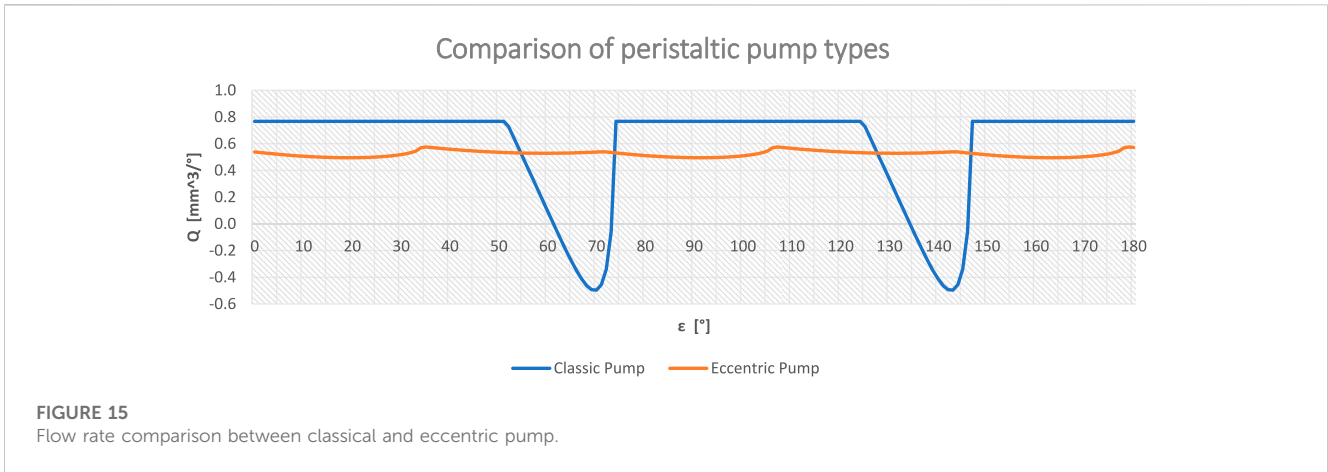


TABLE 1 Indices as roller diameter changes.

Index	$d_{rollers} = 6$	$d_{rollers} = 7$	$d_{rollers} = 8$	$d_{rollers} = 9$	$d_{rollers} = 10$
Irregularity ^a	0.072	0.076	0.080	0.084	0.088
Q average ^a	0.556	0.540	0.525	0.511	0.497
Q average %	72,45	70,34	68,37	66,51	64,76

^a[mm³/s].

$$Q_1 = \Delta V_{liquid\ 1^\circ} - \Delta V_{element} \tag{31}$$

$$Q_2 = \Delta V_{liquid\ 1^\circ} \tag{32}$$

The results of the described relationships are represented on a graph in [Figure 9](#).

Some performance indicators are defined so that results can be evaluated and compared with each other:

Irregularity:

$$Irregularity = Q_{max} - Q_{min} \tag{33}$$

Average flow rate:

$$Q_{average} = \frac{\sum_i Q_i}{n} \tag{34}$$

Average percentual flow rate:

$$Q_{average\ \%} = \frac{Q_{average}}{Q_{max}} \cdot 100 \tag{35}$$

From [Figure 9](#), it can be seen that the flow irregularity is due to the disengagement of the roller from the pipe; in particular, there are some instances when the amount of fluid moved toward the discharge is less than the volume change due to the disengagement, resulting in a negative flow rate, i.e., fluid return.

This trend is caused by the disengagement of the roller in an arc of a very short length ($\approx 22^\circ$). Such behavior is not permissible.

By varying construction parameters such as roller diameter, tube diameter, number of rollers, and rotor diameter, it is possible to limit

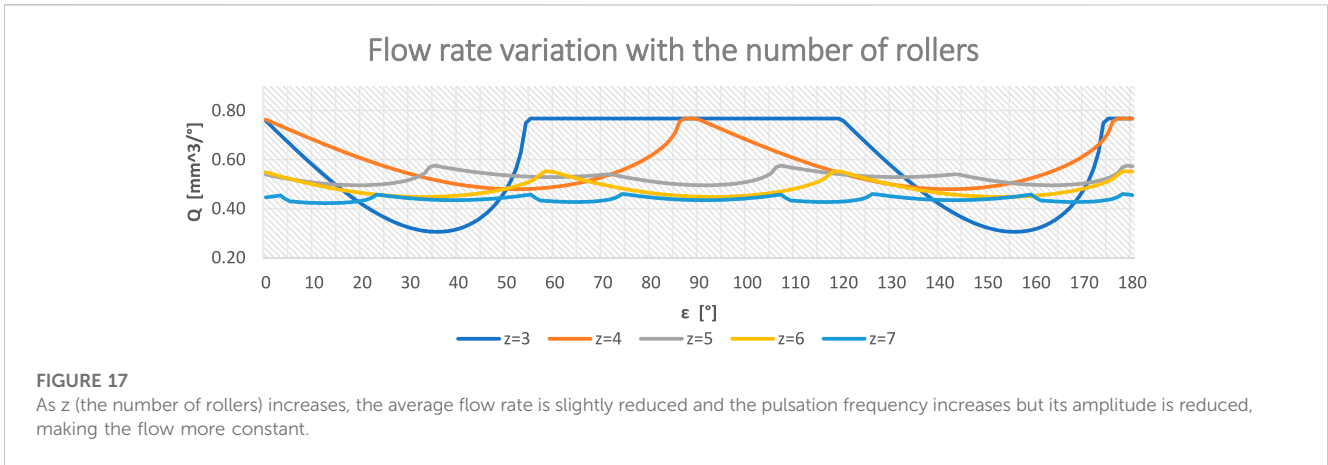


FIGURE 17
As *z* (the number of rollers) increases, the average flow rate is slightly reduced and the pulsation frequency increases but its amplitude is reduced, making the flow more constant.

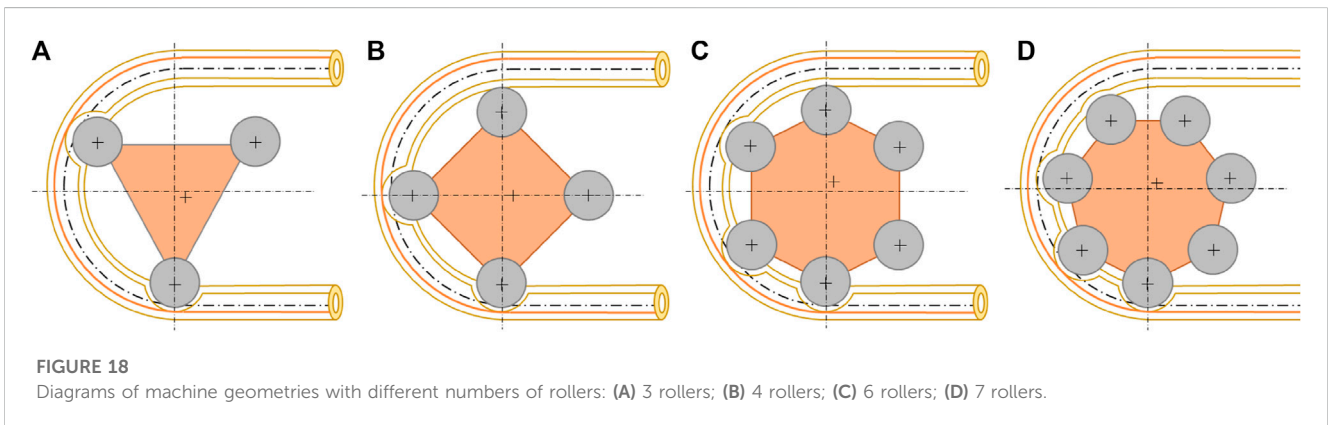


FIGURE 18
Diagrams of machine geometries with different numbers of rollers: (A) 3 rollers; (B) 4 rollers; (C) 6 rollers; (D) 7 rollers.

the amplitude of negative peaks by obtaining a reasonable irregularity and a good average flow rate.

Unfortunately, none of the parameters allow for a constant flow rate or one that can be considered as such, the problem being due to the abrupt disengagement of the roller that generates a major oscillation in the flow rate.

2.2 Displacement and flow rate of eccentric peristaltic pump

The concept behind the new geometry is to increase the disengagement zone to reduce the flow irregularity (Figure 10).

The new geometry consists of a first zone, called the “transfer zone,” with a constant radius of amplitude equal to the angle between two successive rollers (e.g., 5-roller rotor, so $\alpha = 360/z = 72$), which is necessary to isolate the fluid element and prevent the connection between discharge and suction.

The second zone, called the “disengagement zone,” has an eccentric arc to disengage the roller gradually, reducing the irregularity in the flow rate.

A working arc of 180 was also predetermined for this pump geometry so as to have comparable results. From the analyses below

it will be clear whether this geometry really brings advantages over the classical pump.

As can be seen in Figure 10, angle α defines the arc of the case with a constant radius centered in O , and angle θ defines the arc of the case with eccentric geometry with the center in O' :

$$\theta = [0 \div (180 - \alpha)] \tag{36}$$

Defining a generic point of contact P yields the triangle OPO' and applying Carnot’s theorem gives:

$$\rho^2 = r_{case}^2 + e^2 - 2r_{case}e \cos \theta \rightarrow \rho = \pm \sqrt{r_{case}^2 + e^2 - 2r_{case}e \cos \theta} \tag{37}$$

The positive sign must be chosen otherwise it makes no physical sense.

The parameter ρ defines the diameter of the case according to the value of θ and the other geometric parameters. The graphical representation is shown in Figure 11.

In the triangle OPO' , while knowing the angle θ which is referred to O' , one can derive the angle φ because it refers to O and then derive ψ :

$$Se \ \theta < 90^\circ \ \psi = \pi - \arcsin\left(\frac{r_{case}}{\rho} \cdot \sin \theta\right) \tag{38}$$

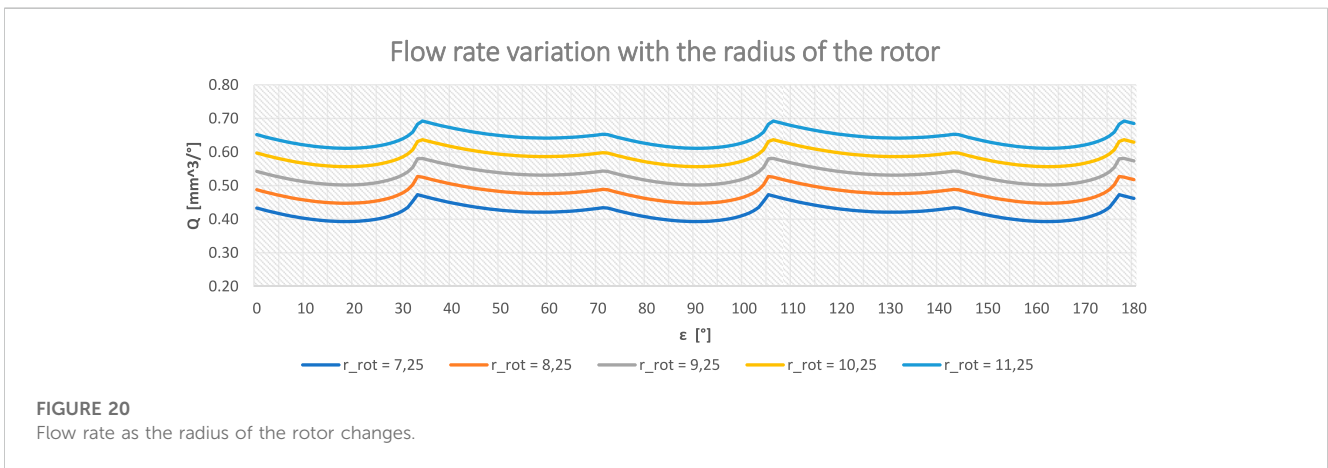
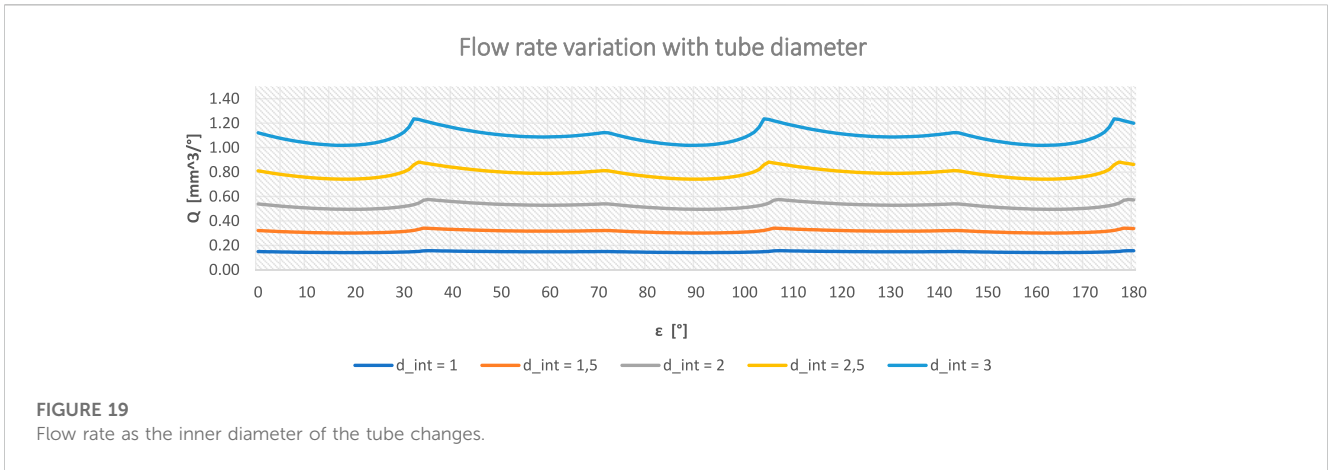


TABLE 2 Indices as the number of rollers changes.

Index	z = 3	z = 4	z = 5	z = 6	z = 7
Irregularity ^a	0.462	0.288	0.080	0.105	0.037
Q average ^a	0.579	0.579	0.525	0.482	0.439
Q average %	75,45	75,45	68,37	62,75	57,16

^a[mm³/°].

TABLE 3 Indices as the inner diameter of the tube changes.

Index	d _{int} = 1	d _{int} = 1,5	d _{int} = 2	d _{int} = 2,5	d _{int} = 3
Irregularity ^a	0.015	0.040	0.080	0.140	0.217
Q average ^a	0.147	0.315	0.525	0.791	1,093
Q average %	76,61	73,00	68,37	65,92	63,29

^a[mm³/°].

$$\text{Se } \theta > 90^\circ \quad \psi = \arcsin\left(\frac{r_{case}}{\rho} \cdot \sin \theta\right) \quad (39)$$

And finally, getting φ :

$$\varphi = 180 - \psi \quad (40)$$

As a verification, Carnot's theorem can be reapplied by referring to the angle φ instead of θ :

$$r_{case}^2 = \rho^2 + e^2 - 2\rho e \cos \psi \quad \rightarrow \quad \rho = -e \cos \phi \pm \sqrt{e^2 (\cos \phi)^2 - (e^2 - r_{case}^2)} \quad (41)$$

The positive sign must be chosen otherwise it makes no physical sense.

To derive the volume of fluid occupied by the roller in all stages of disengagement, as can be seen in Figure 12, it is necessary to know the parameter x :

$$\rho = r_{rotor} + r_{roller} + \left(\frac{d_{ext} - d_{int}}{2}\right) + x \quad (42)$$

$$x = \rho - r_{rotor} - r_{roller} - \left(\frac{d_{ext} - d_{int}}{2}\right) \quad (43)$$

Deriving the b term and finally the a term:

TABLE 4 Indices as rotor radius changes.

Index	$r_{rot} = 7,25$	$r_{rot} = 8,25$	$r_{rot} = 9,25$	$r_{rot} = 10,25$	$r_{rot} = 11,25$
Irregularity ^a	0,0801	0,0799	0,0805	0,0802	0,0813
Q average ^a	0.421	0.476	0.525	0.585	0.640
Q average %	63,98	66,74	68,37	71,15	72,94

^a[mm³/].

$$b = d_{int} - x \tag{44}$$

$$a = \frac{d'}{2} - b \tag{45}$$

At this point, we will refer to the calculations made earlier for the classical peristaltic pump in Eq. (8).

Knowing the volume occupied by the rollers in both the constant-radius phase and the variable-radius phase, it is possible to derive the displacement, which is approximately 11% greater than in the classical pump.

With the new case geometry, the flow rate will be calculated as before, except that the number of rollers that disengage, in some phases, will be more than one at a time (Figure 13).

For clarity, the formulas previously described are given:

$$\Delta V_{liquid\ 1^\circ} = l_{arc\ 1^\circ} \cdot A_{tube} = \frac{\Delta \varepsilon \cdot 2\pi r_{case}}{360} \frac{d_{tubo\ int}^2 \pi}{4} \tag{46}$$

$$\Delta V_{element} = V_{element\ (\varepsilon)} - V_{element\ (\varepsilon+1)} \tag{47}$$

$$Q = \Delta V_{liquid\ 1^\circ} - \Delta V_{tot.\ element} \tag{48}$$

The change in volume due to the gripping rollers varies depending on the angle of the rotor considered.

$$\varepsilon = 0 \div 36^\circ \rightarrow \Delta V_{tot.\ elem.} = \Delta V_B + \Delta V_C \tag{49}$$

$$\varepsilon = 37 \div 72^\circ \rightarrow \Delta V_{tot.\ elem.} = \Delta V_B \tag{50}$$

$$\varepsilon = 72 \div 108^\circ \rightarrow \Delta V_{tot.\ elem.} = \Delta V_B + \Delta V_A \tag{51}$$

$$\varepsilon = 108 \div 144^\circ \rightarrow \Delta V_{tot.\ elem.} = \Delta V_A \tag{52}$$

$$\varepsilon = 144 \div 180^\circ \rightarrow \Delta V_{tot.\ elem.} = \Delta V_A + \Delta V_E \tag{53}$$

In this machine geometry, the transfer zone is reduced to the essentials to ensure no communication between suction and delivery and to maximize the roller disengagement zone from the pipe. Representing the instantaneous flow rate values on a graph yields the following (Figure 14).

The flow rate trend is periodic, with a period defined by the angle between two rollers, which in this case is 72.

3 Results

By comparing the flow rate curves of the two types of pumps, a marked improvement in the pump's flow rate is observed with a drastic reduction in irregularity; by varying some geometric parameters, its operation can be further improved.

In the following, the flow rate as structural parameters of the pump are adjusted will be analyzed by taking advantage of the

representation on graphs (Figure 15) and the indices of irregularity, average flow rate, and average flow rate percentage. Only one parameter will be adjusted at a time to better appreciate its influence.

3.1 Geometric parameters of the eccentric pump

3.1.1 Variation of roller diameter

It can be seen from the graph (Figure 16) that as the roller diameter increases, there is a downward shift in the curve, leading to a reduction in the average flow rate. Since a large roller engaging on the pipe occupies a larger volume of fluid there is a reduction in displacement and flow rate.

Analyzing the indices of the five curves shows that as the diameter of the rollers increases, there is a slight increase in irregularity. Information that cannot be appreciated from the graph is shown in Table 1.

3.1.2 Variation in the number of rollers

There is a significant reduction in irregularity as the number of rollers increases and considering that each roller is a pumping element because it isolates an element of fluid to carry it to the discharge, the rule that a pump with 'pumping elements' of an odd number has less irregularity than one with a higher number of pumping elements internally is verified (Figure 17).

By increasing z, the angle of the transfer zone drops, making the disengagement zone more gradual, thus achieving a reduction in the irregularity of the flow rate (Table 2).

This also results in a reduction in the average flow rate caused by increasing the fluid volume occupied by the rollers gripping the pipe.

Below are diagrams of machines with different numbers of rollers (Figure 18).

A bearing number of less than 3 was not considered because it does not allow the use of this eccentric geometry and we avoided going beyond z = 7 because it would require a larger rotor size and was not justifiable for the reduced improvement in irregularity.

3.1.3 Variation of tube diameter

Increasing the inner diameter of the pipe brings a quadratic increase in the flow rate but with a consequent increase in the irregularity. This is because the volume of fluid occupied by the roller, in a large pipe, is larger than in a small pipe.

For simplicity, the pipe thickness was kept constant in the five cases (Figure 19). In Table 3 the variation of the main indices is summarized.

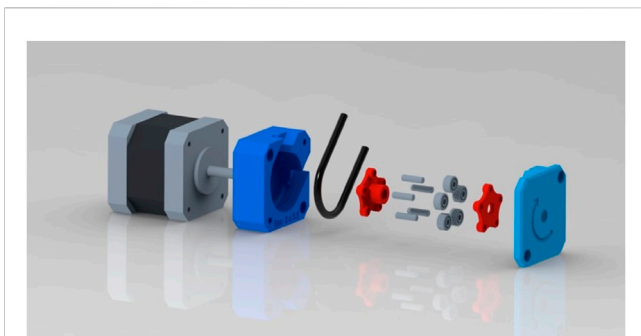


FIGURE 21
Exploded view representation of the pump.

TABLE 5 General properties of PETG.

General properties	Unit	Value	Test method
Specific Gravity	g/cc	1.27	ASTM D792
Moisture Absorption—24 h	%	0.13	ASTM D570
Tensile Strength, Yield	MPa	48	ASTM D638
Tensile Strength, Ultimate	MPa	61	ASTM D638
Elongation at Yield	%	110	ASTM D638
Hardness (Rockwell)	MPa	106	ASTM D2240
Impact Strength (notched Izod, 23C)	kJ/m2	101	ASTM D256
Glass transition temperature	°C	83	ASTM D648

3.1.4 Variation of case and rotor radius

As the rotor radius increases, there is a linear increase in the average flow rate and an almost constant irregularity (Figure 20). This is a useful parameter for increasing the average flow rate of the pump without having to give up good irregularity (Table 4). This is because a rotation of one degree of the rotor in a small case displaces less fluid than in a larger case with the same inner diameter of the tube and bearings. As the size of the rotor varies, the size of the case also varies consistently.

3.2 Realization of the 3D printed prototype

The peristaltic pump is one of the few pumps that can be made with 3D printing because there are no creeping elements that have to make a seal and need tight tolerances, it has few components and has no parts with complex geometries. Moreover, having the liquid inside the tube allows it to transport a fluid that is not akin to the material the pump is made of. Using CAD software, the eccentric pump was made (Figure 21) where all possible components were 3D printed, so the actual operation described and analyzed above could be verified. Given the small size of the prototype made, steel pins were used for the bearings; for larger machines, they could be printed in one piece with one of the two rotor flanges. Fixed wedges could be used as an alternative to rolling rollers; this configuration must provide for excellent lubrication to avoid excessive tube wear and reduced torque from the motor moving the pump.

TABLE 6 Printing parameters.

Parameter	Unit	Value
Layer Height	mm	0.15
Line Width	mm	0.4
Wall Line Count	-	3
Top Layers	-	5
Bottom Layers	-	5
Infill Density	%	15
Printing Temperature	°C	240
Build Plate Temperature	°C	90
Flow	%	95
Print Speed	mm/s	60
Retraction Distance	mm	0.8
Fan Speed	%	100
Regular Fan Speed at Height	mm	3

Polyethylene terephthalate glycol (PETG), a material with fair mechanical properties in the range of 3D printing materials, was chosen, which has the following characteristics (Table 5).

The design of the machine was structured to minimize supports and facilitate printing while minimizing the components to be assembled. The case is made of one piece and attached to the motor by two diametrically opposed screws, the rotor is composed of two flanges that support the pins and rollers that will be housed on the motor shaft via a form fit. Finally, there is the case closure flange, which prevents the tube from slipping out during operation, and is attached by two screws directly to the motor shell. The printing parameters used are as follows (Table 6).

The final 3D printed result is shown in Figure 22.

4 Discussion

As a result of the illustrated analyses, the eccentric geometry of the machine greatly improved its operation. There was constant flow in the branch connected to the roller disengagement zone and the direction of rotation of the pump defined whether it was suction or delivery.

As needed, the same principle can be exploited to achieve both constant suction and delivery of the pump by inserting a part of the eccentric case before and after the constant radius transfer phase, but it is necessary to increase the working arc beyond 180°.

In summary, to further regularize the flow rate of the eccentric pump, one can.

- Reduce the diameter of the bearings;
- Increase the number of rollers;
- Reduce the diameter of the tube;
- Increase the disengagement arc of the rollers.

Table 7 shows the indices referring to the pump types, including two entries for the eccentric pump: the “standard” one uses generic

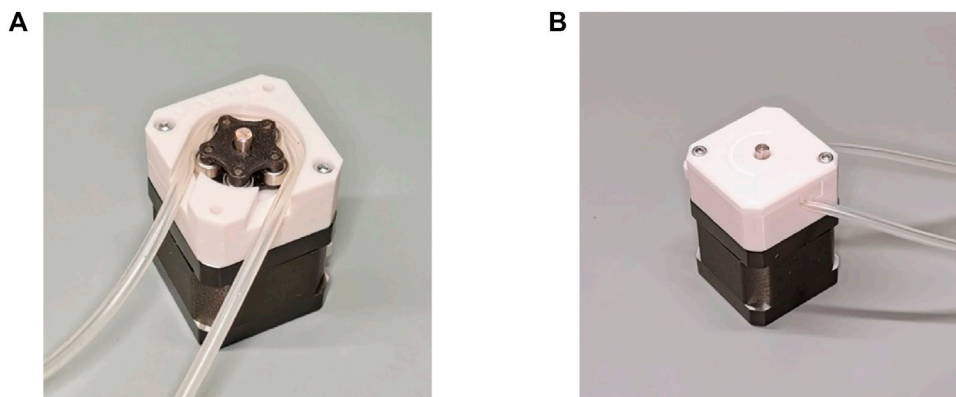


FIGURE 22
Photo of prototype made by 3D printing: (A) Without top flange with rotor and tube in view; (B) With top flange, ready for use.

TABLE 7 Comparison of indices between pump types.

Index	Irregularity ^a	Irregularity %	Q average ^a	Q average %
Classic Pump	1,264	217,7	0.580	75,20
“Standard” Eccentric Pump	0.080	15,34	0.525	68,35
“Plus” Eccentric Pump	0.018	3,72	0.474	76,82

^a[mm³/°].

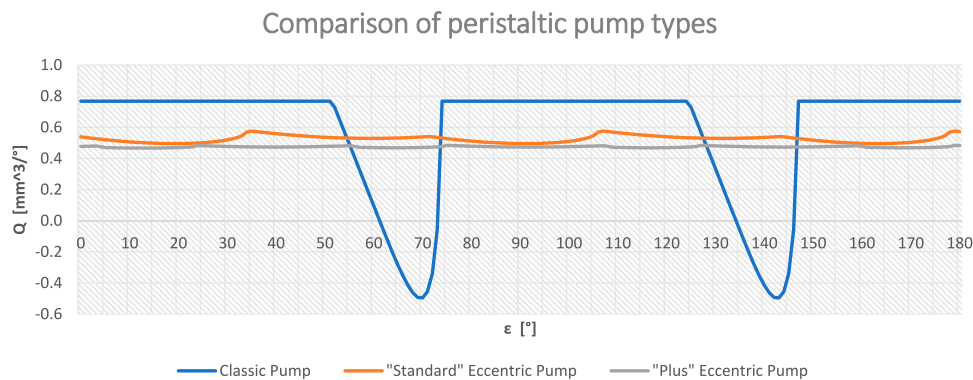


FIGURE 23
Comparison of flow rates among pump types.

parameters for good operation and the “plus” one maximizes the parameters to achieve very little irregularity.

As can be seen from the values in the table, the “standard” eccentric pump has a flow rate with approximately 15 times less irregularity than the classic pump even though there is a slight decrease in the average flow rate.

The “plus” pump allows for a percentage flow rate irregularity of under 5% with a higher average percentage flow rate than the previous geometries. This means that of all the liquid that could flow in the pipe without roller-related obstructions, more than 75% arrives at the discharge; this can be used as a machine efficiency

term. A graph (Figure 23) of the three pump types is also given for completeness.

Comparing the two pumps analyzed previously, and observing the percentage flow rate data, it can be seen that, at the same number of revolutions, the classic pump places approximately 7% more fluid at the delivery than the eccentric one. As a first approximation, the power losses of the two pumps can be considered equal because the materials, parameters, and boundary conditions are the same. It can be said that the classic pump requires less energy than the eccentric pump with the same flow rate delivered but does not allow obtaining a constant outgoing flow.

5 Conclusion

After carrying out various analyses and illustrating the results obtained, it emerged that the inclusion of an eccentricity in the pump body can lead to a considerable improvement in the reduction of the flow rate variability. This means that there is a better chance of using the pump efficiently. The geometry of the pump was parameterized to evaluate the effect on the flow rate by varying the main parameters. This made it easy to understand which modifications would be beneficial for a specific application. For example, reducing the diameter of the pipe can help reduce pulsations in the flow rate, even if this results in a decrease in the average pump flow rate. The pulsation in the flow rate of the classic pump has an irregularity greater than 200%, which leads to various problems within any circuit. With the new eccentric geometry, it is possible to reduce the irregularity by approximately 20 times.

The simple construction and the reduced number of components make the production and maintenance of the pump easy, guaranteeing excellent performance. Furthermore, this opens the door to various industries such as the biomedical, chemical, pharmaceutical, automotive, and aerospace industries. To demonstrate the ease of implementation and geometric feasibility of this type of pump, a working prototype was built using 3D printing technology.

Data availability statement

The original contributions presented in the study are included in the article/supplementary material, further inquiries can be directed to the corresponding author.

References

- Abd-Alla, A. M., Abo-Dahab, S. M., Abdelhafez, M. A., and Thabet, E. N. (2021). Effects of heat transfer and the endoscope on Jeffrey fluid peristaltic flow in tubes. *Multidiscip. Model. Mater. Struct.* 17 (5), 895–914. doi:10.1108/MMMS-12-2020-0292
- Abd-Alla, A. M., Abo-Dahab, S. M., Thabet, E. N., and Abdelhafez, M. A. (2022b). Heat and mass transfer for MHD peristaltic flow in a micropolar nanofluid: Mathematical model with thermophysical features. *Sci. Rep.* 12, 21540. doi:10.1038/s41598-022-26057-6
- Abd-Alla, A. M., Abo-Dahab, S. M., Thabet, E. N., Bayones, F. S., and Abdelhafez, M. A. (2023a). Heat and mass transfer in a peristaltic rotating frame Jeffrey fluid via porous medium with chemical reaction and wall properties. *Alexandria Eng. J.* 66, 405–420. doi:10.1016/j.aej.2022.11.016
- Abd-Alla, A. M., Thabet, E. N., Bayones, F. S., and Alsharif, A. M. (2023b). Heat transfer in a non-uniform channel on MHD peristaltic flow of a fractional Jeffrey model via porous medium. *Indian J. Phys.* 97, 1799–1809. doi:10.1007/s12648-022-02554-2
- Abd-Alla, A. M., Thabet, E. N., and Bayones, F. S. (2022c). Numerical solution for MHD peristaltic transport in an inclined nanofluid symmetric channel with porous medium. *Sci. Rep.* 12, 3348. doi:10.1038/s41598-022-07193-5
- Alessandri, G., Frizziero, L., Santi, G. M., Liverani, A., Dallari, D., Vivarelli, L., et al. (2022). Virtual surgical planning, 3D-printing and customized bone allograft for acute correction of severe genu varum in children. *J. Pers. Med.* 12, 2051. doi:10.3390/JPM12122051
- Abd-Alla, A. M., Abo-Dahab, S. M., Thabet, E. N., and Abdelhafez, M. A. (2022d). Impact of inclined magnetic field on peristaltic flow of blood fluid in an inclined asymmetric channel in the presence of heat and mass transfer. United Kingdom: Waves in Random and Complex Media. doi:10.1080/17455030.2022.2084653
- Abd-Alla, A. M., Abo-Dahab, S. M., Thabet, E. N., and Abdelhafez, M. A. (2022a). Peristaltic pump with heat and mass transfer of a fractional second grade fluid through porous medium inside a tube. *Sci. Rep.* 12, 10608–10614. doi:10.1038/s41598-022-14773-y
- Arockiam, A. J., Subramanian, K., Padmanabhan, R. G., Selvaraj, R., Bagal, D. K., and Rajesh, S. (2022). A review on PLA with different fillers used as a filament in 3D printing. *Mater. Today Proc.* 50, 2057–2064. doi:10.1016/J.MATPR.2021.09.413
- Bachhar, N., Gudadhe, A., Kumar, A., Andrade, P., and Kumaraswamy, G. (2020). 3D printing of semicrystalline polypropylene: Towards eliminating warpage of printed objects. *Bull. Mater. Sci.* 43, 171. doi:10.1007/s12034-020-02097-4
- Bayones, F. S., Abd-Alla, A. M., and Thabet, E. N. (2022). Magnetized dissipative Soret effect on nonlinear radiative Maxwell nanofluid flow with porosity, chemical reaction and Joule heating. United Kingdom: Waves in Random and Complex Media. doi:10.1080/17455030.2021.2019352
- Bayones, F. S., Abd-Alla, A. M., and Thabet, E. N. (2021). Effect of heat and mass transfer and magnetic field on peristaltic flow of a fractional maxwell fluid in a tube. *Complexity* 2021, 1–12. doi:10.1155/2021/9911820
- Chakraborty, D., Prakash, J. R., Friend, J., and Yeo, L. (2012). Fluid-structure interaction in deformable microchannels. *Phys. Fluids* 24, 102002. doi:10.1063/1.4759493
- Chakraborty, S., and Biswas, M. C. (2020). 3D printing technology of polymer-fiber composites in textile and fashion industry: A potential roadmap of concept to consumer. *Compos. Struct.* 248, 112562. doi:10.1016/J.COMPSTRUCT.2020.112562
- Chaturvedi, I., Jandyal, A., Wazir, I., Raina, A., and Ul Haq, M. I. (2022). Biomimetics and 3D printing - opportunities for design applications. *Sensors Int.* 3, 100191. doi:10.1016/j.sintl.2022.100191
- Dave, H. K., and Davim, J. P. (2021). *Fused deposition modeling based 3D printing*. Berlin, Germany: Springer.
- El-Din, M. G., and Rabi, M. (2009). *Fluid power engineering*. New York, NY, USA: McGraw-Hill Education.
- Farooq, N., and Hussain, A. (2022). Peristaltic analysis of Williamson blood flow model with solar biomimetic pump. *Int. Commun. Heat. Mass Transf.* 138, 106305. doi:10.1016/J.ICHEATMASSTRANSFER.2022.106305
- Formato, A., Guida, D., Ianniello, D., Vilecco, F., Lenza, T. L., and Pellegrino, A. (2018). Design of delivery valve for hydraulic pumps. *Mach* 6, 44. doi:10.3390/MACHINES6040044
- Formato, G., Romano, R., Formato, A., Sorvari, J., Koironen, T., Pellegrino, A., et al. (2019). Fluid-structure interaction modeling applied to peristaltic pump flow simulations. *Mach* 7, 50. doi:10.3390/MACHINES7030050

Author contributions

Conceptualization, AM; methodology, PF; software, AM; validation, AM; formal analysis, CP; investigation, AM; resources, AM; data curation, CP; writing—original draft preparation, AM; writing—review and editing, AM and PF; visualization, AM; supervision, AM and PF; project administration, AL and PF; funding acquisition, AL. All authors contributed to the article and approved the submitted version.

Conflict of interest

The authors declare that the research was conducted in the absence of any commercial or financial relationships that could be construed as a potential conflict of interest.

Publisher's note

All claims expressed in this article are solely those of the authors and do not necessarily represent those of their affiliated organizations, or those of the publisher, the editors and the reviewers. Any product that may be evaluated in this article, or claim that may be made by its manufacturer, is not guaranteed or endorsed by the publisher.

- Frizziero, L., Donnici, G., Galìè, G., Pala, G., Pilla, M., and Zamagna, E. (2023). QFD and SDE methods applied to autonomous minibus redesign and an innovative mobile charging system (MBS). *Invent* 8, 1. doi:10.3390/INVENTIONS8010001
- Frizziero, L., Galletti, L., Magnani, L., Meazza, E. G., and Freddi, M. (2022c). Blit vision: Development of a new full-electric sports sedan using QFD, SDE and virtual prototyping. *Inventions* 7, 41. doi:10.3390/INVENTIONS7020041
- Frizziero, L., Leon-Cardenas, C., G. Galìè, G. Alessandri, L. Iannarelli, L. Lucci, et al. (2022b). iDeS method applied to an innovative motorbike—applying topology optimization and augmented reality. *Invent* 7, 91. doi:10.3390/INVENTIONS7040091
- Frizziero, L., Trisolino, G., Santi, G. M., Alessandri, G., Agazzani, S., Liverani, A., et al. (2022a). Computer-aided surgical simulation through digital dynamic 3D skeletal segments for correcting torsional deformities of the lower limbs in children with cerebral palsy. *Appl. Sci.* 12, 7918. doi:10.3390/AP12157918
- Alessandri, G., Santi, G. M., Martelli, P., Guidotti, E., and Liverani, A. (2023). 3D-printing of porous structures for reproduction of a femoral bone, *F1000Research* 12, 17. doi:10.12688/f1000research.129267.1
- Hsu, M. C., Mansouri, M., Ahamed, N. N. N., Larson, S. M., Joshi, I. M., Ahmed, A., et al. (2022a). A miniaturized 3D printed pressure regulator (μ PR) for microfluidic cell culture applications. *Sci. Rep.* 12, 10769. doi:10.1038/s41598-022-15087-9
- Jaffrin, M. Y., and Shapiro, A. H. (1971). Peristaltic pumping. *Annu. Rev. Fluid Mech.* 3, 13–37. doi:10.1146/annurev.fl.03.010171.000305
- Jandyal, A., Chaturvedi, I., Wazir, I., Raina, A., and Ul Haq, M. I. (2022). 3D printing – a review of processes, materials and applications in industry 4.0. *Sustain. Operations Comput.* 3, 33–42. doi:10.1016/j.susoc.2021.09.004
- Kafle, A., Luis, E., Silwal, R., Pan, H. M., Shrestha, P. L., and Bastola, A. K. (2021). 3D/4D printing of polymers: Fused deposition modelling (FDM), selective laser sintering (SLS), and stereolithography (SLA). *Polym* 13, 3101. doi:10.3390/POLYM13183101
- Kaplan, D. E., Burkett, D., and Warden, L. (2018). *United States patent: 4909710A*.
- Karassik, I. J., Messina, J. P., Cooper, P., and Heald, C. C. (2008). *Pump handbook*. New York, NY, USA: McGraw-Hill Education.
- Khandpur, R. S. (2003). *Handbook of biomedical instrumentation*. New York, NY, USA: Tata McGraw-Hill.
- Kristiawan, R. B., et al. Kristiawan, R. B., Imaduddin, F., Ariawan, D., Ubaidillah Arifin, Z. (2021). A review on the fused deposition modeling (FDM) 3D printing: Filament processing, materials, and printing parameters. *OEng* 11, 639–649. doi:10.1515/ENG-2021-0063
- Kumar, B., Raina, A., Singh, R. P., and Haq, M. I. U. (2022). “Mechanical properties for 3D printing of polymers through fused deposition modelling,” in *Optimization of industrial systems*. Editors D. Panchal, M. Tyagi, A. Sachdeva, and D. Pamucar (Hoboken, NJ, USA: Wiley online library). doi:10.1002/9781119755074.ch27
- Kunz, G., Beil, D., Deiniger, H., Einspanier, A., Mall, G., and Leyendecker, G. (1997). The uterine peristaltic pump: Normal and impeded sperm transport within the female genital tract. *Adv. Exp. Med. Biol.* 424, 267–277. doi:10.1007/978-1-4615-5913-9_49/COVER
- Latham, T. W. (1966). Fluid motions in a peristaltic pump. Available at: <https://dspace.mit.edu/handle/1721.1/17282> (accessed March 20, 2023).
- Liu, C., Ho, C., and Wang, J. (2018). The development of 3D food printer for printing fibrous meat materials. *IOP Conf. Ser. Mater. Sci. Eng.* 284, 012019. doi:10.1088/1757-899X/284/1/012019
- Mora, A., Verma, P., and Kumar, S. (2020). Electrical conductivity of CNT/polymer composites: 3D printing, measurements and modeling. *Compos. Part B Eng.* 183, 107600. doi:10.1016/J.COMPOSITESB.2019.107600
- Elabbasi, N., Bergstrom, J., and Brown, S. (2011). Fluid-structure interaction analysis of a peristaltic pump, *Proceedings of the 2011 COMSOL Conf.* 1–4. Burlington, MA, February 2011.
- Raza, M. H., Zhong, R. Y., and Khan, M. (2022). Recent advances and productivity analysis of 3D printed geopolymers. *Addit. Manuf.* 52, 102685. doi:10.1016/J.ADDMA.2022.102685
- Romero, P. E., Arribas-Barrios, J., Rodriguez-Alabanda, O., González-Merino, R., and Guerrero-Vaca, G. (2021). Manufacture of polyurethane foam parts for automotive industry using FDM 3D printed molds. *CIRP J. Manuf. Sci. Technol.* 32, 396–404. doi:10.1016/J.CIRPJ.2021.01.019
- Rouf, S., Raina, A., Ul Haq, M. I., Naveed, N., Jeganmohan, S., and Kichloo, A. F. (2022). 3D printed parts and mechanical properties: Influencing parameters, sustainability aspects, global market scenario, challenges and applications. *Adv. Industrial Eng. Polym. Res.* 5 (3), 143–158. doi:10.1016/j.aiepr.2022.02.001
- Saunier, J., Khzam, A., and Yagoubi, N. (2022). Impact of mechanical stress on flexible tubing used for biomedical applications: Characterization of the damages and impact on the patient's health. *J. Mech. Behav. Biomed. Mater.* 136, 105477. doi:10.1016/J.JMBBM.2022.105477
- Sausse, A. (2018). *United States patent: 3784323A*.
- Shapiro, A. H., Jaffrin, M. Y., and Weinberg, S. L. (1969). Peristaltic pumping with long wavelengths at low Reynolds number. *J. Fluid Mech.* 37, 799–825. doi:10.1017/S0022112069000899
- Turton, R. K. (1994). *Rotodynamic pump design*. Cambridge, UK: Cambridge University Press. doi:10.1017/CBO9780511529573
- Volk, M. (2013). *Pump characteristics and applications*. Boca Raton, Florida: CRC Press.
- Wang, P., Zou, B., Ding, S., Li, L., and Huang, C. (2020). Effects of FDM-3D printing parameters on mechanical properties and microstructure of CF/PEEK and GF/PEEK. *Chin. J. Aeronaut.* 34, 236–246. doi:10.1016/j.cja.2020.05.040
- Weinberg, S. L., Eckstein, E. C., and Shapiro, A. H. (1971). An experimental study of peristaltic pumping. *J. Fluid Mech.* 49, 461–479. doi:10.1017/S0022112071002209
- Wickramasinghe, S., Do, T., and Tran, P. (2020). FDM-based 3D printing of polymer and associated composite: A review on mechanical properties, defects and treatments. *Polym* 12, 1529. doi:10.3390/POLYM12071529